



# Influence of Reduced Graphene Oxide (rGO) on Plasma Sprayed Nanostructured Coatings

Akella Srikanth<sup>1</sup> · Venkateshwarlu Bolleddu<sup>1</sup>

Submitted: 9 March 2022 / in revised form: 17 January 2023 / Accepted: 30 January 2023 / Published online: 27 February 2023  
© ASM International 2023

**Abstract** The effect of the addition of reduced graphene oxide (rGO) in atmospheric plasma-sprayed nanostructured  $\text{Al}_2\text{O}_3$ -13wt.% $\text{TiO}_2$  and WC-25wt.%Co coatings was studied by varying the percentage weight proportion of rGO as 0.5, 1, and 1.5wt.%. The reason for adding rGO is that some critical issues such as brittleness, cracking can limit the applications of plasma sprayed coatings. Graphene being one of the allotropes of carbon, it has attracted great interest in recent times as a reinforcement for composite coatings due to its exceptional strength. To overcome the problems associated with plasma-sprayed coatings, the addition of reduced graphene oxide (rGO) as an additive is considered one of the best solutions to improve the characteristics and properties of these coatings. After the coatings were deposited and characterized, it was observed that the percentage of porosity in the coatings gradually decreases with increasing proportion of rGO. In addition, it was also noticed that the presence of rGO in the microstructure of the coatings increases the resistance to crack propagation due to the formation of a bridge between the bond coat and the top coat, thus improving the fracture resistance of the coatings.

**Keywords** air plasma spraying · alumina-titania · nanostructured coatings · reduced graphene oxide · tungsten carbide-cobalt

## Introduction

In the recent past, thermal barrier coatings (TBCs) have received significant attention toward surface engineering applications due to their duplex-type structure consisting of metallic bond coats and ceramic top coats. The metallic bond coat protects the substrate material from corrosive and oxidative attacks, whereas the ceramic topcoat reduces the temperature of substrates because of its lower thermal conductivity and increases the lifetime of components (Ref 1, 2). Air plasma spraying (APS) is a well-known coatings deposition technique on parts used for corrosion and wear resistance applications (Ref 3, 4). Also, due to its superior properties, APS is widely used for coatings deposition on turbine blades, aircraft engines, plungers, nozzle pumps, etc. (Ref 5-8).  $\text{Al}_2\text{O}_3$  is the most significant and commonly used anti-wear ceramic material that can be deposited using the plasma spraying technique, but the drawback is that pure  $\text{Al}_2\text{O}_3$  is having inadequate toughness. Adding a proper volume of  $\text{TiO}_2$  into  $\text{Al}_2\text{O}_3$  ceramics to make  $\text{Al}_2\text{O}_3$ - $\text{TiO}_2$  compounds enhances the toughness, bonding strength, and compactness (Ref 9-12). Generally,  $\text{Al}_2\text{O}_3$ -13 wt.%  $\text{TiO}_2$  can exhibit good hardness and toughness, and hence it is used in many applications like boiler nozzles, turbine blades, etc. (Ref 13-15). In thermally sprayed WC-Co ceramic coatings, the hard tungsten-carbide (WC) works as the wear-resistant material and the cobalt (Co) acts as a binder to provide toughness for the coatings. Due to these superior properties, thermally sprayed WC-Co coatings are widely used in many engineering applications where resistance to sliding, abrasion, erosion, and fretting is required (Ref 16, 17).

However, APS-sprayed alumina ceramic coatings (95  $\text{Al}_2\text{O}_3$ , 2 wt.%  $\text{SiO}_2$  and 3 wt.% others) obtained at a spray distance of 12 cm with a thickness of 100  $\mu\text{m}$  acquire a

✉ Venkateshwarlu Bolleddu  
venkateshwarlu.b@vit.ac.in; venkatsoft2004@gmail.com

<sup>1</sup> Department of Manufacturing, School of Mechanical Engineering, Vellore Institute of Technology, Vellore 632014, India

greater microhardness ( $HV_{0.3} = 1215 \text{ kg/mm}^2$ ) and minimum porosity of 4.1% with a minimum surface roughness of  $4.18 \mu\text{m}$  (Ref 18). Lower and higher spray distances other than 12 cm resulted in lower hardness, the high porosity and the high coating roughness. It was reported that longer spray distance increases the dwell time in the plume and allows more heating/melting of powder particles and thus produce most dense coatings. Also, this plasma sprayed alumina coatings suffer from a few critical concerns like brittleness, cracking, etc., that are limiting their applications. This is happening, especially in ceramic coatings due to the lack of protective layer formation that controls the coefficient of friction during the abrasion (Ref 19–21). To overcome this problem, in recent times, the coatings are reinforced with additives because of their unique features like including high wear resistance, high hardness, low friction coefficient, and good thermal stability, thus significantly improves the service life under high-temperature working conditions (Ref 22). Reduced graphene oxide (rGO) is one of the best additive alternatives available.

Graphene is a formation of single-layer carbon atoms possessing a 2D-hexagonal structure, and it has been attracted widely in major industrial applications due to its unique features like high specific surface area, thermal stability, chemical resistance, and gases impermeability, etc., (Ref 23–26). Also, graphene is the thinnest material, and it can exhibit the highest thermal conductivity of  $3000 \text{ W m}^{-1} \text{ K}^{-1}$ , and electrical conductivity of  $2.5 \times 10^5 \text{ cm}^2 \text{ V}^{-1} \text{ s}^{-1}$  (Ref 27). Furthermore, it has superior mechanical properties (1 TPa Young's modulus and 130 GPa intrinsic strength) (Ref 28). These properties made graphene a potential material for coating applications (Ref 23, 29). However, using graphene alone as the coating is very difficult due to its single-layer formation, and it cannot protect the surface completely.

Schrifer et al. (Ref 30) investigated the characteristics of graphene-reinforced Cu metal coatings deposited using the chemical vapor deposition (CVD) process. It was found that there were many defects on the surface due to oxidation. On the contrary, it also accelerated the corrosion process. A possible solution to prevent this kind of issue is using graphene-based oxides (Ref 31–33). Because of having multilayers, the graphene-based oxides are highly impermeable to liquids, gases, and vapors (Ref 34, 35). Therefore, the graphene and its oxides can be deposited as coatings on the surfaces of metal substrates such as steel, copper alloy, aluminum alloy, magnesium alloy, titanium, nickel, (Ref 36, 37). A major difference between GO and rGO structures is the specific surface area. GO shows relatively a lower surface area (i.e.,  $890 \text{ m}^2 \text{ g}^{-1}$ ) in comparison to the rGO structure which almost restores the extremely high surface area of pristine graphene

( $\sim 2600 \text{ m}^2 \text{ g}^{-1}$ ). The mechanical strength of GO is also found to be lower than the mechanical strength of the rGO structure. Young's modulus of GO is found to be almost half of rGO and graphene. GO structures show hydrophilic behavior, while rGO shows hydrophobic behavior due to the loss of oxygen-containing compounds (Ref 38). Due to these reasons, reduced graphene oxide (rGO) doped coatings are widely used as an anti-friction and wear-resistant material on Ti-based alloys in mechanical systems and devices than graphene oxide. Also, a significant improvement in the wear resistance had been noticed in coatings added with rGO (Ref 39). The rGO is nothing but a purified form of GO. It can be obtained by reducing oxygen-related functional groups of graphene oxide through thermal or chemical processing techniques. However, there were no such studies have been carried out to investigate the microstructural characteristics and mechanical properties of the APS-sprayed nanostructured coatings reinforced with rGO.

In this research work, Air plasma sprayed (APS) nanostructured  $\text{Al}_2\text{O}_3$ -13TiO<sub>2</sub> and WC-25wt.%Co coatings reinforced with rGO are obtained and characterized to investigate the powder morphology, coating microstructure, phases present in powder and coatings, porosity, and bond strength of the coatings.

## Experimental Procedure

Two types of nanostructured ceramic feedstock powders, namely  $\text{Al}_2\text{O}_3$ -13 TiO<sub>2</sub> and WC-25 wt.%Co, were used to obtain the air plasma sprayed coatings. In addition, the nanostructured reduced graphene oxide (rGO) was added in these powders in three different percentage proportions by weight (i.e., 0.5, 1, and 1.5 wt.%) to study the effect of rGO reinforcement on the microstructural characteristics and mechanical properties of the obtained coatings. The parameters used for the deposition of the APS sprayed coatings are shown in Table 1.

**Table 1** Parameters used for deposition of coatings

Parameter	Range
Voltage	65–75 V
Current	430–480 A
Flow rate of primary gas (Ar)	100–115 l/min
Flow rate of carrier gas (H <sub>2</sub> )	10–13 l/min
Powder feed rate	50–60 g/min
Stand-off distance (SOD)	60–100 mm

## Sample Preparation and Coatings Deposition

The mild steel substrates (AISI 1020) of  $100 \times 100 \times 6$  mm were used for coatings deposition. First, the substrates were ground using a surface grinder (Alex NH 500) to remove the oxide layers and excess dirt present on the surface of the substrates. About  $0.1 \mu\text{m}$  surface roughness was maintained on the substrate surface after grinding. Later, using alumina grits with an average grit size of 28, the substrates were grit blasted at 140 psi air pressure, and then substrate samples were ultrasonically cleaned in an acetone bath for 25 min to remove the dust and other unwanted foreign particles. Finally, the substrates were preheated up to  $200 \text{ }^\circ\text{C}$  before coatings deposition.

The coatings were deposited in a reputed industry in India: *Spraymet Surface Technologies, Private Limited, Bangalore, India*. Sulzer Metco 3 MB plasma gun was used for depositing coatings with argon as the primary plasma gas and hydrogen as the secondary carrier gas. Firstly, the bond coat of Ni-10 wt.%CrAlY was deposited with a thickness ranging from 140 to  $170 \mu\text{m}$ , and later the top coatings of  $\text{Al}_2\text{O}_3$ -13  $\text{TiO}_2$  and WC-25 wt.%Co were deposited with an average thickness of about  $250 \mu\text{m}$ . The nanostructured powders of  $\text{Al}_2\text{O}_3$ -13  $\text{TiO}_2$ , WC-25 Co, and rGO were obtained from *Nano Research Lab, Jamshedpur, Jharkhand, India*. It can be noted that the nanostructured  $\text{Al}_2\text{O}_3$ -13  $\text{TiO}_2$  and WC-25 wt.%Co powders with an average size of  $20$ – $45 \mu\text{m}$  were mixed properly with rGO having an average size of  $35$ – $50 \mu\text{m}$  using a ball milling process (at 180 rpm for 1 h) in three different weight percentage proportions of 0.5, 1, and 1.5 wt.%. It can be noted that the tap densities of nanostructured  $\text{Al}_2\text{O}_3$ -13  $\text{TiO}_2$ , WC-25 wt.%Co, and rGO are 3.5, 3.9, and  $1.91 \text{ g/cm}^3$ , respectively.

Further, the cross-sectional specimens of size  $10 \times 5 \times 6$  mm were cut using a low-speed diamond saw to investigate the characteristics of the obtained coatings. For metallographic studies, the cross-sectional specimens were hot-mounted using Bakelite powder. These hot-mounted samples were polished with SiC abrasive sheets of grades 220, 400, 600, 800, and 1000. Polishing was done with each grade of an abrasive sheet for 10 min duration, and later, the disk polishing was done for 15 min on all the samples.

## Characterization and Analysis

For microstructure analysis, the microstructure of the coatings on the cross-sectional specimen was observed using Zeiss Evo 18 scanning electron microscope (SEM). For each variant of coatings, seven images at various magnifications were taken. X-ray diffraction (XRD) studies

were performed on PAN analytical X' pert PRO (PW1070) x-ray diffractometer with radiation of  $\text{CuK}\alpha$  with 40 kV operating voltage, 40 mA current, step time of 0.14 s, and scanning step of  $0.0172^\circ$ , and the phases were analyzed from the obtained XRD data. The percentage porosity of the coatings was estimated using several SEM micrographs that were captured. Also, the image analysis software *Image J* was used to adjust the contrast variation between the voids and other features in the coating microstructure.

The bond strength tests were conducted as per ASTM C633 standards at *Virtue meta-sol, Private Limited, Hyderabad, India*. The cylindrical test pieces with a diameter of 25.4 mm and a height of 38.1 mm were prepared to examine the bond strength of the coatings. The coated cylindrical face of the substrate was attached with a dummy (uncoated) cylinder using ultra-bond epoxy glue. The dummy samples were placed on top of the epoxy glue in an inverted position. Thermal curing was performed at the temperature of  $205 \pm 2 \text{ }^\circ\text{C}$  for 4 hs after epoxy gluing. After curing, coupling of the coated and dummy epoxy cylinders was started using the Instron 5969 model universal testing machine (UTM) with a capacity of 50 kN.

## Results and Discussion

### Powder Morphologies and Phase Analysis

The powder morphologies of nanostructured  $\text{Al}_2\text{O}_3$ -13  $\text{TiO}_2$  and WC-25 wt.%Co powders were investigated through SEM analysis without and with reduced graphene oxide (rGO) addition in three different weight percentage proportions: 0.5, 1, and 1.5 wt.%. Since the rGO was mixed properly with the ball milling process, the uniform distribution of rGO has been noticed throughout the powders in the corresponding SEM micrographs.

### Powders Morphology before Adding rGO

The morphology of nanostructured  $\text{Al}_2\text{O}_3$ -13 wt.% $\text{TiO}_2$  feedstock powder before adding the rGO is shown in Fig. 1(a). It is shown in Fig. 1(a) that Alumina-Titania powder particles have a regular and nearly spherical shape with nonuniform particle size. Also, the powder particles seem to have few pores as these powders are prepared by spray drying and sintering techniques. The porous nature of agglomerated powders results in lower thermal diffusivities and is expected to partially melt some of the powder particles. It may be noted that nanostructured agglomerated  $\text{Al}_2\text{O}_3$ -13 wt.% $\text{TiO}_2$  powders have a tap density of  $1.4 \text{ g/cm}^3$  (information on tap density for nanostructured powders is provided by the manufacturer). Scanning electron microscopy (SEM) image for nanostructured tungsten

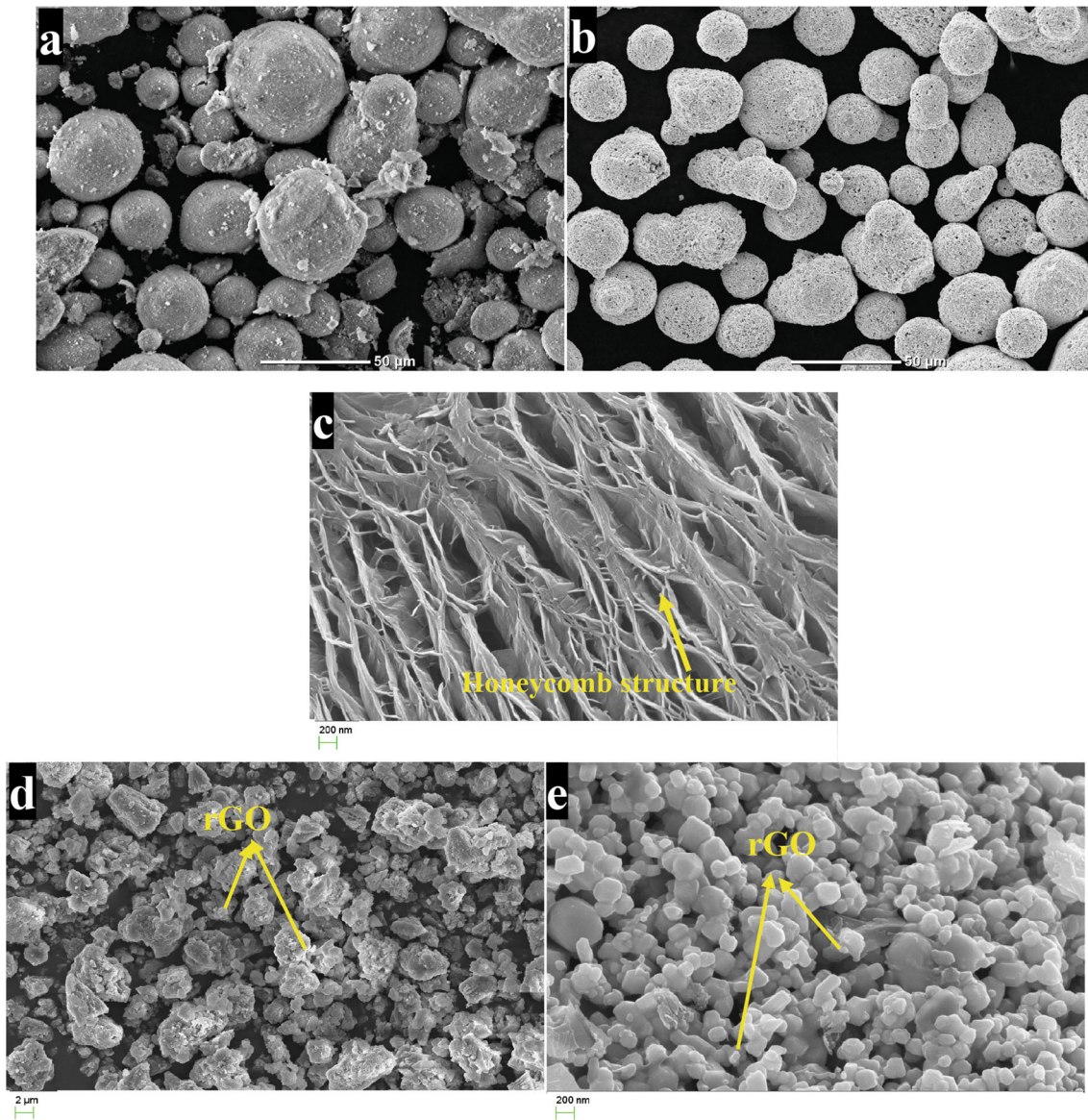


**Fig. 1** Powder morphology of nanostructured (a)  $\text{Al}_2\text{O}_3$ -13wt.% $\text{TiO}_2$ , (b) WC-25% Co, (c) rGO, (d)  $\text{Al}_2\text{O}_3$ -13wt.% $\text{TiO}_2$  mixed with 1.5% rGO, (e) WC-25% Co mixed with 1.5% rGO

carbide-cobalt feedstock powder morphology without adding the rGO is shown in Fig. 1(b). It can be observed that these powder particles are hollow and have regular, spherical shape morphology with almost uniform particle size. However, these powder particles seem to be more porous than nanostructured  $\text{Al}_2\text{O}_3$ -13 wt.% $\text{TiO}_2$  powder particles (See Fig. 1b). It can be noted that, during air plasma spraying, the porous and hollow nature of nanostructured powders is expected to result in more decomposition at a higher temperature of spraying and dissolution of the WC phase, making the corresponding coatings less tough.

The morphology of rGO powder particles is shown in Fig. 1(c). It can be observed in Fig. 1(c) that rGO powder

particles have a honeycomb microstructure that increases the bond strength and reduces friction. The folded-type structure of rGO is shown in Fig. 1(c). In addition, the folded structure is happening in rGO due to oxygen functional-related groups (Ref 40). Further, an extra folded and wrinkled structure can be observed in rGO when it is well-built and become tougher (Ref 41).

#### Powders Morphology after Adding rGO

The morphology of nanostructured  $\text{Al}_2\text{O}_3$ -13 wt.% $\text{TiO}_2$  and WC-25 wt.%Co feedstock powders after mixing with rGO are examined thoroughly using SEM, and corresponding images are shown in Fig. 1. It is shown in

Fig. 1(d) that after adding the rGO powder, the spherical-shaped alumina-titania powder particles have become more agglomerated. It is considered that the agglomeration of spherical shape powders could minimize inter-particle resistance and reduce nozzle clogging, which is essential for achieving high-density and uniform coatings (Ref 42, 43). Also, it has been noticed that these agglomerated powders result in an enhanced flow of powders during the deposition of coatings (Ref 44). Similarly, the morphology of nanostructured WC-25wt.%Co powder after adding the rGO is shown in Fig. 1(e). Furthermore, it is shown in Fig. 1(e) that the rGO has been mixed with tungsten carbide powder particles uniformly. The Laplace equation explains this uniform mixing of rGO with  $\text{Al}_2\text{O}_3$ -13TiO<sub>2</sub> and WC-25wt.%Co feedstock powders, which derives that while reducing the radius of nano-sized particles, it will become unstable and distributed over these feedstock powders uniformly (Ref 45). Thus, this uniform mixing results in lower porosity of powder (Ref 46).

### Phase Analysis of Powder

The phases present in the composition of nanostructured alumina-titania and tungsten carbide-cobalt feedstock powders are determined using the x-ray diffraction (XRD) analysis, and the corresponding XRD patterns are shown in Fig. 2. It is shown in Fig. 2(a) that nanostructured  $\text{Al}_2\text{O}_3$ -13wt.%TiO<sub>2</sub> powder has  $\alpha$ -alumina and anatase titania as the major phases in it. However, after adding the rGO, the presence of a new graphite phase with less intensity has also been found (See Fig. 2b). The  $\alpha$ -alumina phase present in the powder provides high-temperature resistance, and also, the tetragonal crystal structure of anatase-titania gives

additional strength to  $\alpha$ -alumina (Ref 47–49). Peak broadening can be noticed in  $\alpha$ -alumina and anatase titania phases signifying the presence of micro-stresses, varying from point to point in both phases. Similarly, the x-ray diffraction (XRD) patterns for nanostructured tungsten carbide-cobalt feedstock powders are shown in Fig. 2. It is shown in Fig. 2(c) that only WC and Co crystalline phases are present as the major phases in nanostructured agglomerated tungsten carbide-cobalt powders. It is also observed that the cobalt phase has a lower intensity than the WC phases, and it is attributed to the lower percentage proportion in the powder composition. However, after adding the rGO, a different graphite phase is also observed, as shown in Fig. 2(d).

### Coatings Microstructure and Phase Distribution

#### $\text{Al}_2\text{O}_3$ -13wt.%TiO<sub>2</sub> Coatings

The cross-sectional SEM micrographs of nanostructured  $\text{Al}_2\text{O}_3$ -13wt.%TiO<sub>2</sub> coating are shown in Fig. 3. In Fig. 3(a), the typical architecture of plasma sprayed coating having topcoat, bond coat, and substrate is shown. In Fig. 3(b) the top coating microstructure without rGO addition represents the partially melted (PM) and fully melted (FM) regions. The partially melted regions and the fully melted regions form the bi-modal microstructure that can control the cracks propagation, particularly at the interfaces in the nanostructured coatings (Ref 6, 50, 51). The cross-sectional view of 1.5wt.% rGO added  $\text{Al}_2\text{O}_3$ -13wt.%TiO<sub>2</sub> coating is shown in Fig. 3(c). The microstructure of the top coating with rGO addition is shown in Fig. 3. From Fig. 3(d), it can also be observed

**Fig. 2** Phase analysis of (a)  $\text{Al}_2\text{O}_3$ -13wt.%TiO<sub>2</sub> powder without rGO, (b)  $\text{Al}_2\text{O}_3$ -13wt.%TiO<sub>2</sub> powder with 1.5wt.% rGO, (c) WC-25wt.%Co powder without rGO, (d) WC-25wt.%Co powder with 1.5wt.% rGO

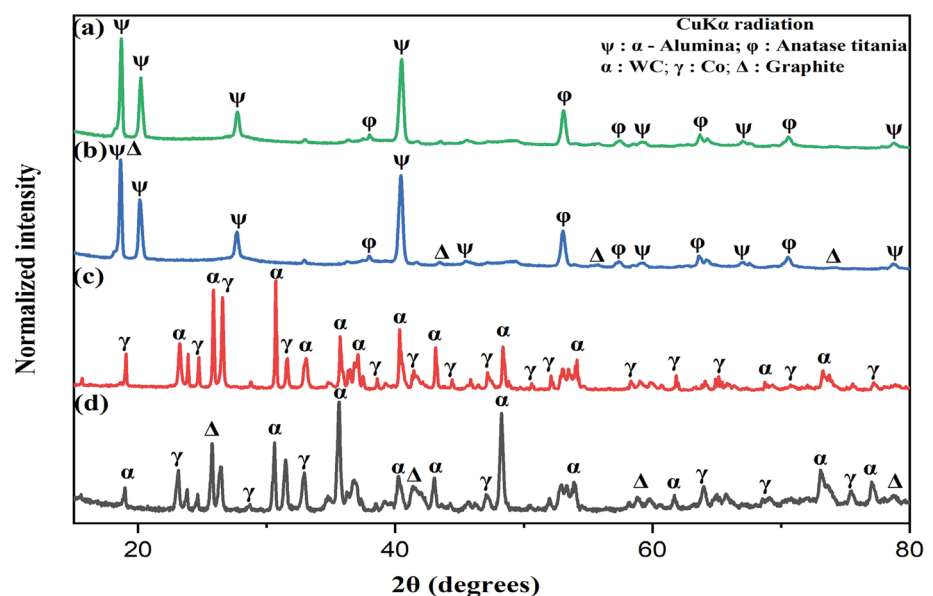
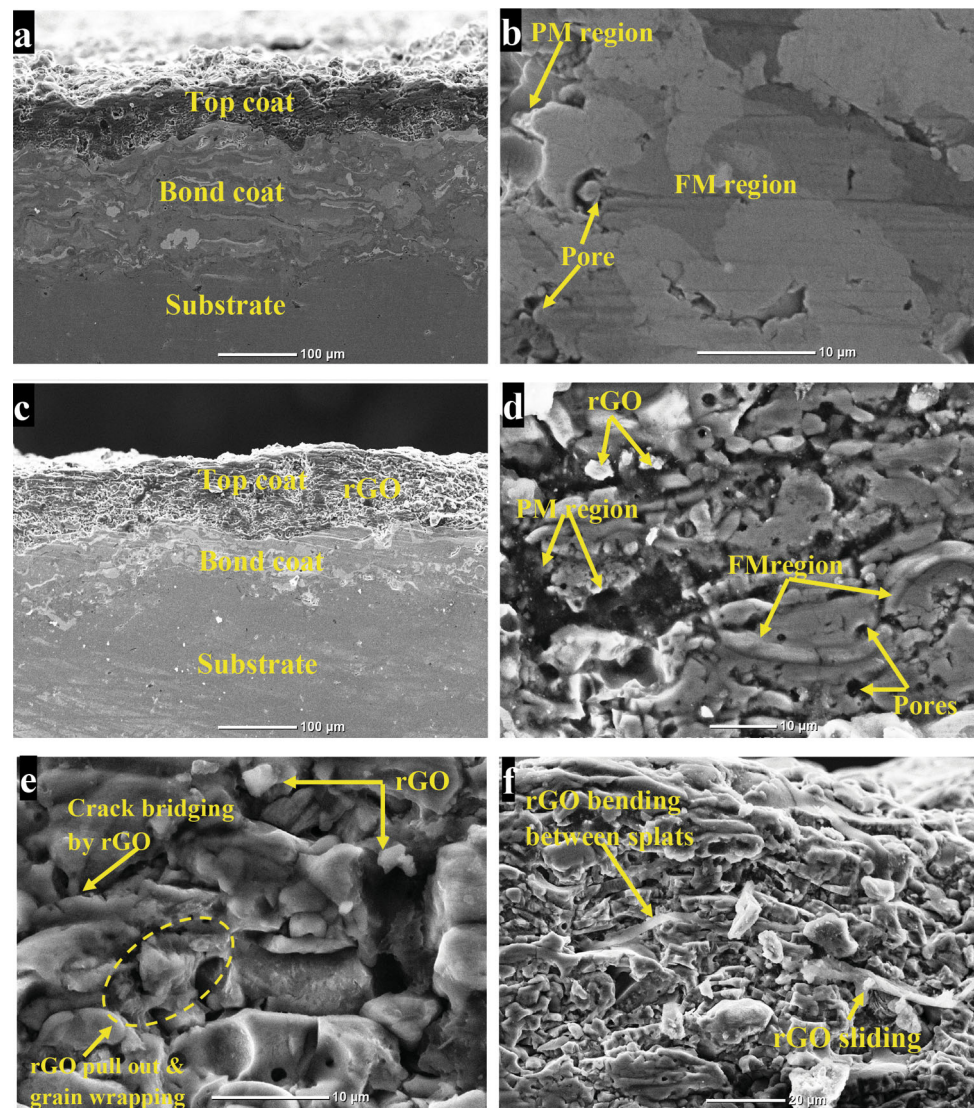


**Fig. 3** Coating microstructure of  $\text{Al}_2\text{O}_3$ -13wt.% $\text{TiO}_2$  (a) without rGO addition two layers of coating, (b) without rGO addition top coating, (c) with 1.5wt.% rGO addition two layers of coating (a) top coating with 0.5wt.% rGO, (b) top coating with 1.0wt.% rGO, (c) top coating with 1.5wt.% rGO



that the coating microstructure has fully melted (FM) and partially melted (PM) regions in its microstructure. It is shown in Fig. 3(e) that there are some pores in the microstructure of the 0.5wt.% rGO added coatings, and the rGOs act as a bridge between the cracks. It is believed that as the rGO is having larger surface area than CNT (Carbon nanotube), rGOs crack bridging is more efficient in delaying the crack propagation. Crack initiation through the rGO bridge requires more energy, which indicates an increase in the fracture toughness of the coatings. Figure 3(e) shows the rGO pullout that requires the dissipation of more fracture energy as it is having a higher interfacial area on the external force application. Therefore, the toughness increases automatically which can delay the fracture in the coatings. Figure 3(e) also displays the grain wrapping by rGO that can oppose the crack initiation efficiently by holding the grains jointly in the partially

melted regions (PM regions) and re-solidified areas (Ref 52). Further, it is evident from Fig. 3(f) that there is rGO bending between the splats and sliding on the splats due to its lubricant nature.

The XRD patterns of nanostructured  $\text{Al}_2\text{O}_3$ -13wt.% $\text{TiO}_2$  coatings with and without the addition of rGO are shown in Fig. 4. It is shown in Fig. 4(a) that alumina is present in the form of  $\alpha$ -alumina and  $\gamma$ -alumina, whereas titania is present in the form of rutile and magneli phases in the microstructure of coatings. It can also be observed that the anatase titania phase present in the powder has disappeared completely and converted into rutile and magneli phases in the microstructure of coatings (Ref 53). The rutile titania phase is a more stable form of  $\text{TiO}_2$  at all temperatures than the anatase titania phase. The magneli phase of titania has occurred at high temperatures due to the reduction in titania. Also, some of  $\alpha$ -alumina has been transformed into

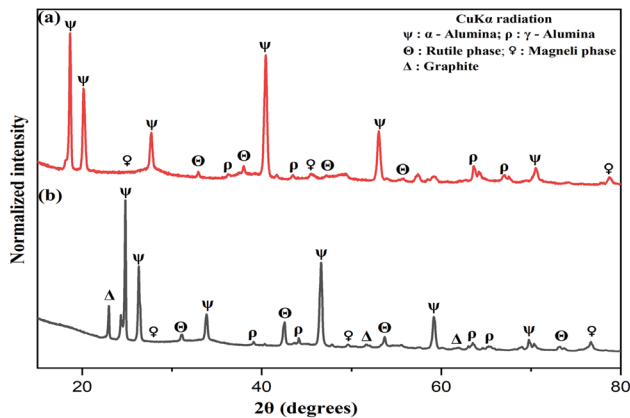


**Fig. 4** Phase analysis of  $\text{Al}_2\text{O}_3$ -13wt.% $\text{TiO}_2$  coatings: (a) without rGO, (b) with 1.5wt.% rGO

$\gamma$ -alumina after the deposition of coating (Ref 54, 55). It can also be observed that the graphite phase present in the powder form is still retained even after the coating deposition (See Fig. 4b).

#### WC-25wt.%Co Coatings

The cross-sectional SEM images showing the microstructure of nanostructured WC-25wt.%Co coatings are shown in Fig. 5. It shows the typical coating architecture with WC-25wt.%Co topcoat microstructure and the presence of bond coat on the substrate. Figure 5(d) shows the microstructure of 0.5wt.% rGO mixed WC-25wt.%Co coatings. The fully melted (FM) and partially melted (PM) regions that form the bimodal microstructure are observed in the coating microstructure, as shown in Fig. 5(d). This bi-modal microstructure of coatings controls the crack propagation at the coating interfaces. The presence of a few pores in the coating microstructure is also observed. Figure 5(e) shows the microstructure of 1.0 wt.% rGO mixed WC-25wt.%Co coatings. It is observed that the rGO has been formed as the glue at the splat interfaces and resists crack propagation (Ref 56). Also, Fig. 5(e) shows that the rGO is embedded and glued into the WC-25wt.%Co splats. This scenario occurred at the time of the air plasma spraying (layer-by-layer deposition) process. The splat gluing in between rGO and WC-25wt.%Co particles has a high bonding force, which gradually enhances the fracture toughness. The same observation of graphene nanoparticles splat gluing with alumina coatings in plasma sprayed coatings was identified by Mukherjee et al. (Ref 56). Figure 5(e) shows the rGO bending between the splats and it occurred mainly due to the high-velocity collision of powder particles during plasma spraying. Both rGO sliding and bending follow the mechanism of energy dissipation which requires more energy for crack initiation. The same behavior is reported by Neito et al. (Ref 57), and it was observed that the increased fracture toughness of

coatings is due to both graphene nanoparticles sliding and bending (Ref 57).

Figure 5(f) shows the microstructure of 1.5 wt.% rGO mixed WC-25wt.%Co coatings. It can be observed that there is rGO pullout and grain wrapping that increase the toughness of coating (Ref 58). Further, the sliding phenomenon between the splats is observed due to the collision of particles to the substrate with high velocity at the time of plasma spraying that increases the toughness of the coating [see Fig. 5(f)] (Ref 57).

The phases present in the microstructure of WC-25wt.%Co coatings obtained without and with the addition of rGO are shown in Fig. 6. It is observed that the coatings obtained without the addition of rGO consist of tungsten carbide (WC), Cobalt (Co), and semi-tungsten carbide ( $\text{W}_2\text{C}$ ) phases as the major phases in its microstructure (see Fig. 6a). Compared to the phases present in the feedstock powder, an additional phase of semi-tungsten carbide ( $\text{W}_2\text{C}$ ) is also observed in the coating microstructure. This  $\text{W}_2\text{C}$  phase is formed due to decarburization at a higher temperature during thermal spraying. However, the remaining phases WC and Co, are also retained in the coating microstructure. Further, in rGO-added WC-25wt.%Co coatings, the graphite phase is observed along with the phases mentioned above [see Fig. 6b].

#### Porosity

The porosity of the APS coatings obtained with and without rGO addition is evaluated using multiple micrographs of coatings microstructure, and the corresponding bar graphs are shown in Fig. 7(a) and (b). It is observed from Fig. 7(a) and (b) that in both the coatings of  $\text{Al}_2\text{O}_3$ -13 $\text{TiO}_2$  and WC-25wt.%Co, the porosity is changing with variation in the percentage proportion of rGO. It is observed from Fig. 7(a) that the  $\text{Al}_2\text{O}_3$ -13wt.% $\text{TiO}_2$  coatings obtained without rGO addition have the highest porosity of  $9.1 \pm 0.1\%$ . But,  $\text{Al}_2\text{O}_3$ -13wt.% $\text{TiO}_2$  coatings obtained with 1.5wt.% rGO addition show minimum percentage porosity of  $6.5 \pm 0.2\%$ . Similarly, it is observed from Fig. 7(b) that the WC-25wt.%Co coatings obtained without rGO addition have the highest porosity of  $7.4 \pm 0.2\%$ . However, WC-25wt.%Co coatings obtained with 1.5wt.% rGO addition shows minimum percentage porosity of  $5.8 \pm 0.2$ . It has been observed from Fig. 7(a) and (b) that the coatings obtained with 1.5wt.% rGO addition have the lowest percentage of porosity. It can also be seen that the percentage of porosity has been decreasing gradually with an increasing percentage of rGO addition. This phenomenon is attributed to the filling of rGO in the micropores present in the coating microstructure (Ref 7).

It can be seen that the percentage porosity is decreasing gradually with an increasing percentage of rGO addition in

**Fig. 5** Coating microstructure of WC-25wt.%Co (a) without rGO addition two layers of coating, (b) without rGO addition top coating, (c) with 1.5wt.% rGO addition two layers of coating (a) top coating with 0.5wt.% rGO, (b) top coating with 1.0wt.% rGO, (c) top coating with 1.5wt.% rGO

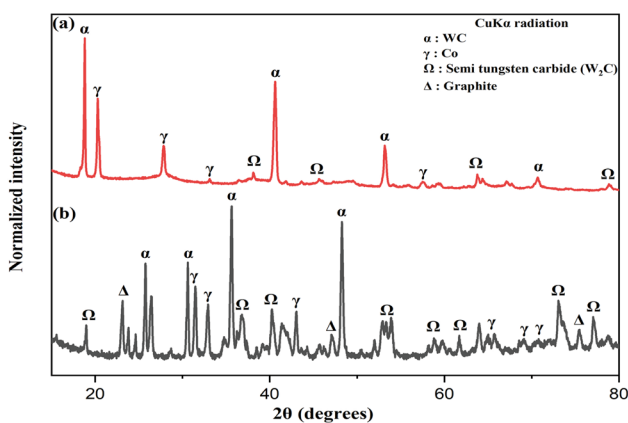
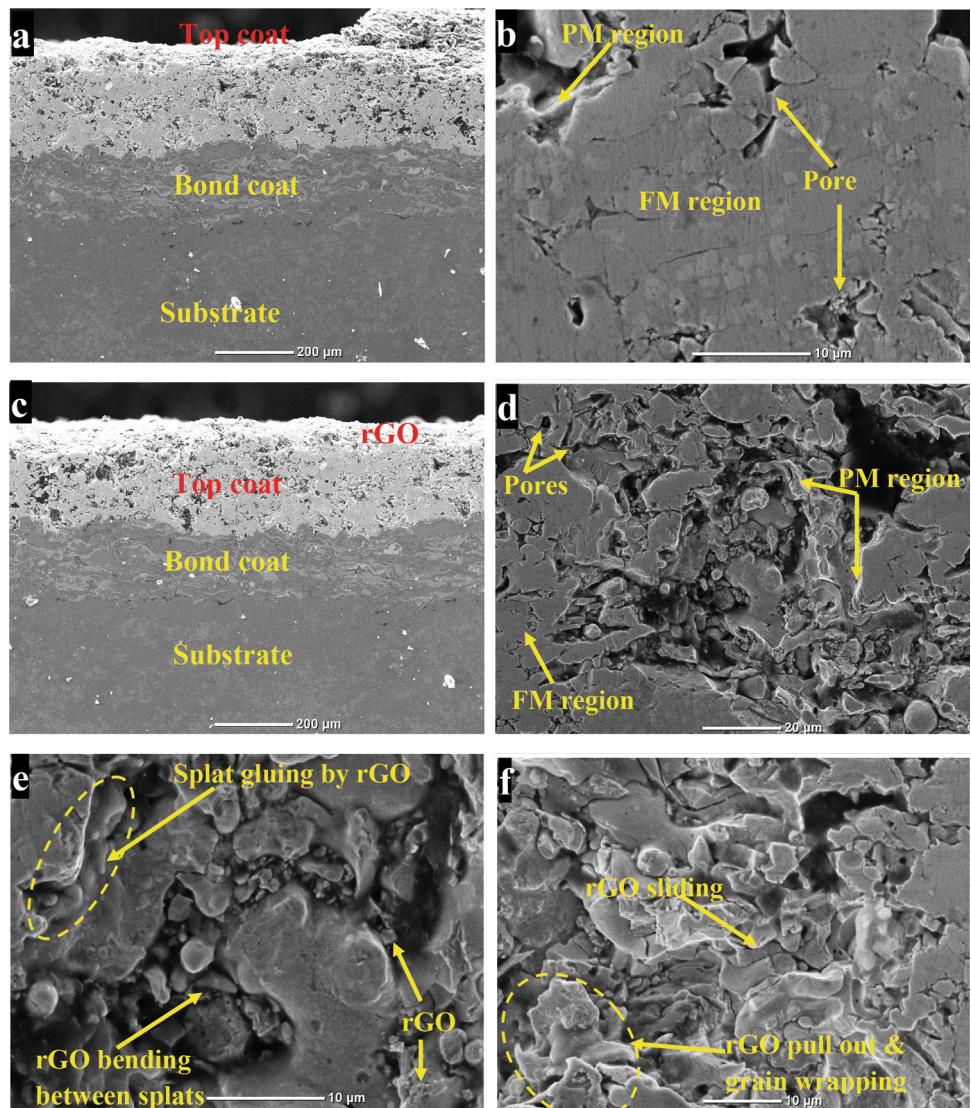


**Fig. 6** Phase analysis of WC-25wt.%Co coatings: (a) without rGO, (b) with 1.5wt.% rGO

both  $\text{Al}_2\text{O}_3\text{-13TiO}_2$  and WC-25wt.%Co coatings. The reduction in porosity of rGO-added coatings could be because of two reasons. Firstly, the inter-splat region is the main source of porosity which can be easily filled by rGO particles. Secondly, the rGO particles are having higher thermal conductivity as compared to the  $\text{Al}_2\text{O}_3\text{-13TiO}_2$  and WC-25wt.%Co powders. (Ref 59, 60). At the time of coatings deposition, the powders are melted easily due to higher thermal conductivity, and hence well distributed dense coatings are obtained. As a result of this, a lower percentage of porosity is obtained in the APS sprayed coatings. Also, it can be noted that a minor decrease in the porosity level could have a significant impact on various properties of the coatings such as mechanical properties and crystalline nature (Ref 58).



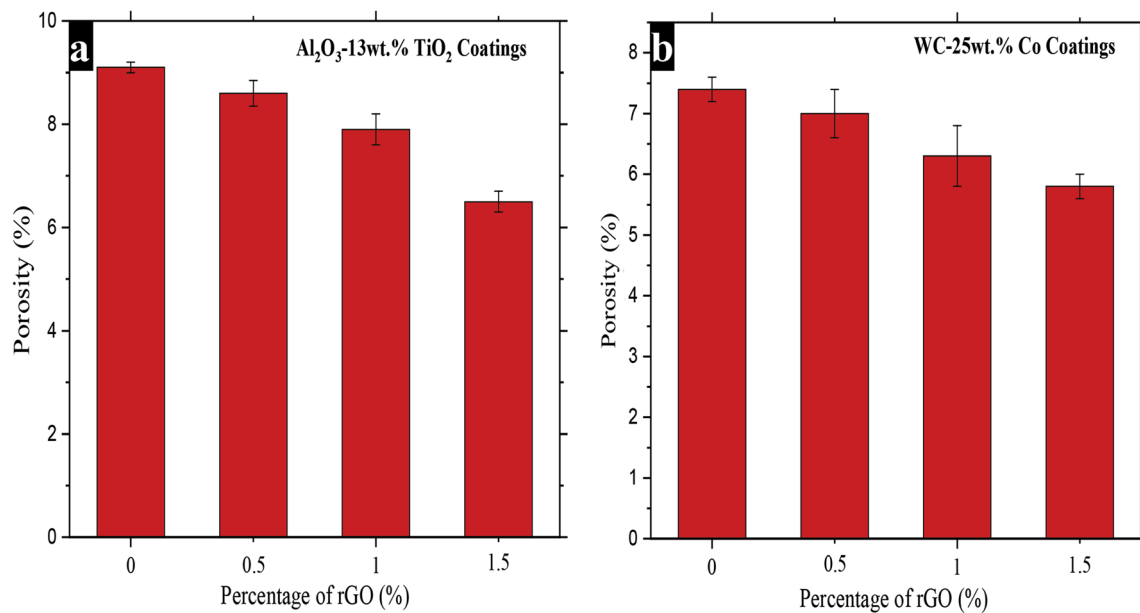


**Fig. 7** Porosity variation of: (a) Al<sub>2</sub>O<sub>3</sub>-13wt.%TiO<sub>2</sub> coatings, (b) WC-25wt.%Co coatings as a function of rGO percentage

### Bond Strength

The coating strength has also been evaluated in the bond strength tests. The fractured surfaces of Al<sub>2</sub>O<sub>3</sub>-13wt.%TiO<sub>2</sub> coated samples are shown in Fig. 8(a), and it can be observed that the coating failure that occurred during the bond test is cohesion failure resulting from the inter-splat failure. The bond strength tests show that the highest bond strength of coating mainly depends on the coating roughness and the load applied on the coating (Ref [61]).

The increase in the percentage proportion of rGO is enhancing the bond strength of Al<sub>2</sub>O<sub>3</sub>-13TiO<sub>2</sub> and WC-25wt.%Co coatings gradually. When the bonding strength increases gradually, corresponding residual stresses decreases. The increase in the bonding strength in Al<sub>2</sub>O<sub>3</sub>-13TiO<sub>2</sub> and WC-25wt.%Co coatings is due to the accumulation of less amount of residual stresses that usually develop during the coatings deposition process due to the solidification and spreading of molten particles (Ref [62, 63]).

The bond strength variation of coatings as a function of rGO addition is shown in Fig. 8(b) and (c). It is observed that the bond strength of APS sprayed Al<sub>2</sub>O<sub>3</sub>-13TiO<sub>2</sub> and WC-25wt.%Co coatings obtained without adding the rGO is the lowest as compared to the coatings obtained with rGO addition, and its magnitude is obtained as  $36.65 \pm 0.8$  MPa and  $41.71 \pm 0.96$  MPa, respectively. However, the Al<sub>2</sub>O<sub>3</sub>-13TiO<sub>2</sub> and WC-25wt.%Co coatings obtained with 1.5wt.% rGO addition have shown a maximum bond strength of  $42.86 \pm 0.54$  and  $47.92 \pm 0.83$  MPa, respectively (see Fig. 8b and c). Thus, it can be observed that increasing the

percentage proportion of rGO is enhancing the bond strength of coatings gradually.

### Conclusions

The rGO mixed air plasma-sprayed Al<sub>2</sub>O<sub>3</sub>-13TiO<sub>2</sub> and WC-25wt.%Co coatings were obtained and characterized to investigate the powder morphology, coating microstructure, phase analysis, percentage porosity, and bond strength of the coatings. In this work, rGO was added to the feedstock powders in the weight percentage proportions of 0.5, 1, and 1.5. Based on the results obtained from the experimental investigation, the following conclusions can be drawn.

- (1) The wedge-shaped Al<sub>2</sub>O<sub>3</sub>-13wt.%TiO<sub>2</sub> and spherical-shaped WC-25Co nanostructured powders have turned less porous after adding the rGO.
- (2) The XRD analysis of nanostructured Al<sub>2</sub>O<sub>3</sub>-13wt.%TiO<sub>2</sub> powder exhibits  $\alpha$ -Alumina and anatase titania phases as the major phases present. But WC-25wt.%Co powder exhibits tungsten carbide (WC) and cobalt (Co) as the major phases. In addition, after adding rGO to these powders, a different phase of graphite was also observed.
- (3) The nanostructured coatings exhibited bi-modal microstructure consisting of fully melted (FM) regions and partially melted (PM) regions that can reduce the cracks propagation in the coatings and enhances their fracture toughness.

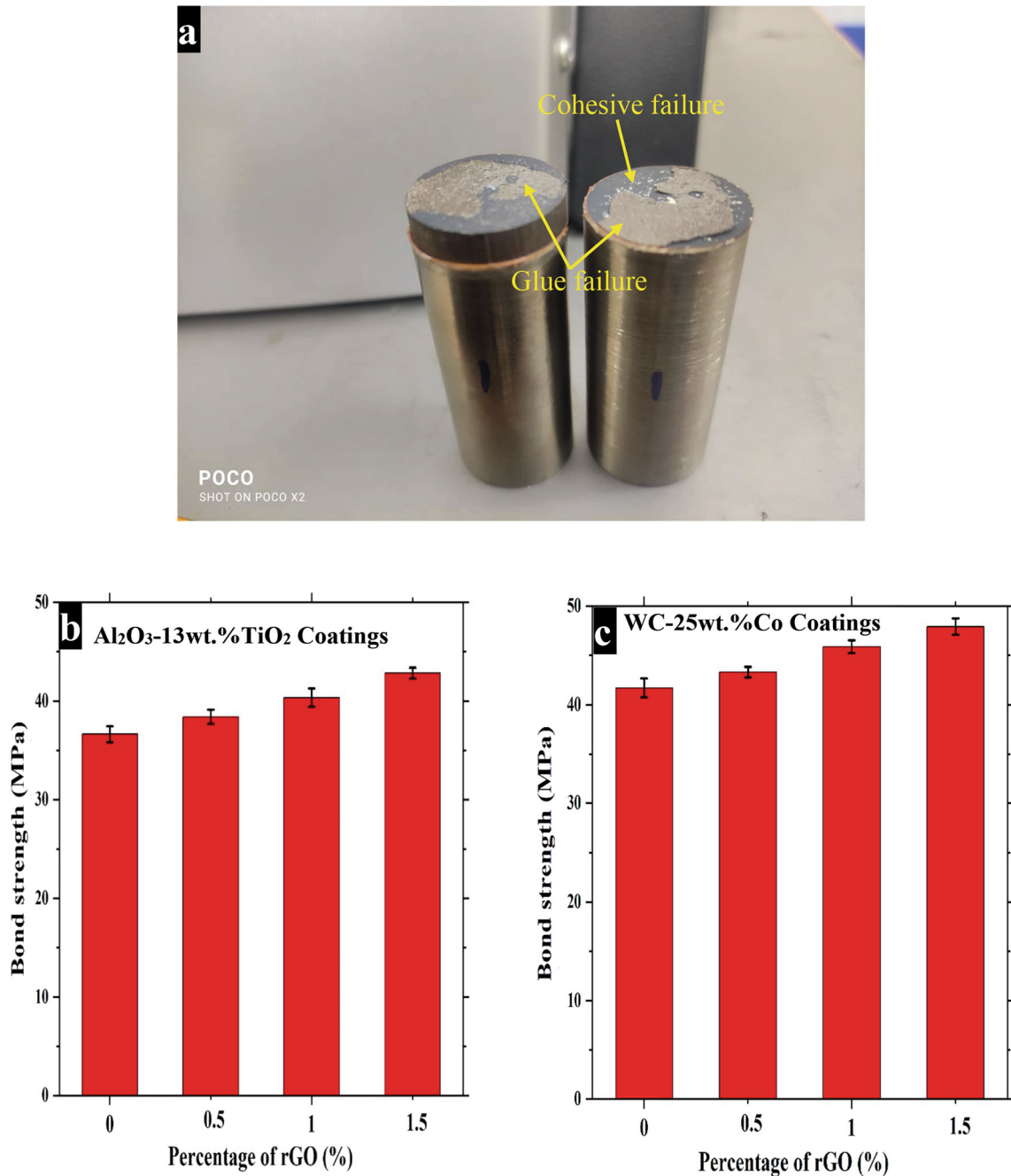


**Fig. 8** (a) Fractured surface of  $\text{Al}_2\text{O}_3\text{-13wt.\%TiO}_2$  coated sample in bond strength test; Bond strength variation in: (b)  $\text{Al}_2\text{O}_3\text{-13wt.\%TiO}_2$  coatings, (c) WC-25wt.%Co coatings as a function of rGO percentage

- (4) The presence of rGO in the microstructure of coatings has been increasing the crack propagation resistance by forming a bridge between the bond coat and topcoat. Also, rGO exhibits the sliding nature between splats due to its lubricant nature, and thus reduces the top coat friction.
- (5) The percentage porosity of both  $\text{Al}_2\text{O}_3\text{-13TiO}_2$  and WC-25wt.%Co nanostructured coatings has been

- reduced with the increasing percentage of rGO due to lessening of the pores and smoothing of the surface.
- (6) The bond strength of coatings showed that the addition of rGO made the coatings more resistant to crack formation and crack propagation by forming the bridges between the cracks and wrapping on the splats to enhance the performance of the coatings.

**Acknowledgments** Dr. B. Venkateshwarlu and A. Srikanth acknowledge the Science and Engineering Research Board (SERB), Department of Science and Technology (DST), New Delhi, India, for providing financial support to this research work via Project No.: EEQ/2017/000096.

## References

1. R. Vaßen, M.O. Jarligo, T. Steinke, D.E. Mack, and D. Stöver, Overview on Advanced Thermal Barrier Coatings, *Surf. Coat. Technol.*, 2010, **205**(4), p 938-942. <https://doi.org/10.1016/j.surfcoat.2010.08.151>
2. V. Arnault, R. Mevrel, S. Alperine, and Y. Jaslier, Thermal Barrier Coatings for Aircraft Turbine Airfoils: Thermal Challenge and Materials, *Revue de Métallurgie*, 1999, **96**(5), p 585-597. <https://doi.org/10.1051/metal/199996050585>
3. G.M.T. Basha, A. Srikanth, and B. Venkateshwarlu, Effect of Reinforcement of Carbon Nanotubes on Air Plasma Sprayed Conventional Al<sub>2</sub>O<sub>3</sub>-3% TiO<sub>2</sub> Ceramic Coatings, *Mater. Today Proc.*, 2020, **20**, p 191-194. <https://doi.org/10.1016/j.matpr.2019.11.025>
4. G. Bolelli, V. Cannillo, R. Gadow, A. Killinger, L. Lusvardi, and J. Rauch, Properties of High Velocity Suspension Flame Sprayed (HVSFS) TiO<sub>2</sub> Coatings, *Surf. Coat. Technol.*, 2009, **203**(12), p 1722-1732. <https://doi.org/10.1016/j.surfcoat.2009.01.006>
5. K. Balani and A. Agarwal, Process Map for Plasma Sprayed Aluminum Oxide—Carbon Nanotube Nanocomposite Coatings, *Met. Finish.*, 2008, **106**(10), p 45-51. [https://doi.org/10.1016/S0026-0576\(08\)80204-8](https://doi.org/10.1016/S0026-0576(08)80204-8)
6. Y. Wang, S. Jiang, M. Wang, S. Wang, T.D. Xiao, and P.R. Strutt, Abrasive Wear Characteristics of Plasma Sprayed Nanostructured Alumina/Titania Coatings, *Wear*, 2000, **237**(2), p 176-185. [https://doi.org/10.1016/S0043-1648\(99\)00323-3](https://doi.org/10.1016/S0043-1648(99)00323-3)
7. G.M.T. Basha and B. Venkateshwarlu, Influence of CNTs in Protecting Air Plasma Sprayed Al<sub>2</sub>O<sub>3</sub>-3wt%TiO<sub>2</sub> Coated Surface, in *IOP Conference. Series: Materials Science Engineering*, IOP Publishing, 1123(1), 012065, (2021) doi:<https://doi.org/10.1088/1757-899X/1123/1/012065>.
8. G.T. Basha and V. Bolleddu, Impact of Carbon Nanotubes Reinforcement on Microstructural and Tribological Characteristics of Air Plasma Sprayed Conventional Alumina-Titania (Al<sub>2</sub>O<sub>3</sub>-3wt%TiO<sub>2</sub>) Coatings, *Iran. J. Mater. Sci. Eng.*, 2020 <https://doi.org/10.22068/ijmse.17.3.92>
9. R. Yilmaz, A.O. Kurt, A. Demir, and Z. Tatl, Effects of TiO<sub>2</sub> on the Mechanical Properties of the Al<sub>2</sub>O<sub>3</sub>-TiO<sub>2</sub> Plasma Sprayed Coating, *J. Eur. Ceram. Soc.*, 2007, **27**(2), p 1319-1323.
10. S. Jia, Y. Zou, J. Xu, J. Wang, and L. Yu, Effect of TiO<sub>2</sub> Content on Properties of Al<sub>2</sub>O<sub>3</sub> Thermal Barrier Coatings by Plasma Spraying, *Trans. Nonferrous Metals Soc. China*, 2015, **25**(1), p 175-183.
11. F. Vargas, H. Ageorges, P. Fournier, P. Fauchais, and M.E. López, Mechanical and Tribological Performance of Al<sub>2</sub>O<sub>3</sub>-TiO<sub>2</sub> Coatings Elaborated by Flame and Plasma Spraying, *Surf. Coat. Technol.*, 2010, **205**(4), p 1132-1136.
12. G.M. Thalib Basha, A. Srikanth, and B. Venkateshwarlu, A Critical Review on Nano Structured Coatings for Alumina-Titania (Al<sub>2</sub>O<sub>3</sub>-TiO<sub>2</sub>) Deposited by Air Plasma Spraying Process (APS), *Mater. Today Proc.*, 2020, **22**, p 1554-1562.
13. P. Manae, Z. Valefi, and M. Goodarz, The Effect of Bond Coat Type on the Stab Resistance of Al<sub>2</sub>O<sub>3</sub>-13 Wt% TiO<sub>2</sub> Plasma Sprayed Ceramic Coating on Aramid Fabrics, *Surf. Interfaces*, 2020, **18**, p 100432.
14. M. Wang, Z. Zhou, Y. Yi, and Z. Wang, Thermal-Shock Resistance of Plasma Sprayed Al<sub>2</sub>O<sub>3</sub>-13 Wt %TiO<sub>2</sub> Coating Evaluated by Residual Strength Method, *Surf. Coat. Technol.*, 2019, **375**, p 888-893.
15. S. Mehar, S.G. Sapate, N. Vashishtha, and P. Bagde, Effect of Y<sub>2</sub>O<sub>3</sub> Addition on Tribological Properties of Plasma Sprayed Al<sub>2</sub>O<sub>3</sub>-13% TiO<sub>2</sub> Coating, *Ceram. Int.*, 2020, **46**(8), p 11799-11810.
16. S.F. Wayne and S. Sampath, Structure/Property Relationships in Sintered and Thermally Sprayed WC-Co, *JTST*, 1992, **1**(4), p 307-315.
17. H.J. Kim, Y.G. Kweon, and R.W. Chang, Wear and Erosion Behavior of Plasma-Sprayed WC-Co Coatings, *JTST*, 1994, **3**(2), p 169-178.
18. O. Sarikaya, Effect of Some Parameters on Microstructure and Hardness of Alumina Coatings Prepared by the Air Plasma Spraying Process, *Surf. Coat. Technol.*, 2005, **190**(2), p 388-393. <https://doi.org/10.1016/j.surfcoat.2004.02.007>
19. R.S. Lima and B.R. Marple, Superior Performance of High-Velocity Oxyfuel-Sprayed Nanostructured TiO<sub>2</sub> in Comparison to Air Plasma-Sprayed Conventional Al<sub>2</sub>O<sub>3</sub>-13TiO<sub>2</sub>, *J. Therm. Spray Tech.*, 2005, **14**(3), p 397-404. <https://doi.org/10.1361/105996305X59413>
20. J.J. Kang, B.S. Xu, H.D. Wang, and C.B. Wang, Influence of Contact Stress on Rolling Contact Fatigue of Composite Ceramic Coatings Plasma Sprayed on a Steel Roller, *Tribol. Int.*, 2014, **73**, p 47-56. <https://doi.org/10.1016/j.triboint.2013.12.019>
21. K. Torkashvand, S. Joshi, and M. Gupta, Advances in Thermally Sprayed WC-Based Wear-Resistant Coatings: Co-Free Binders Processing Routes and Tribological Behavior, *J. Therm. Spray Tech.*, 2022, **31**(3), p 342-377.
22. G. Zhao, J. Wang, Y. Deng, T. Yan, W. Liang, T. Li, L. Zhang, Q. Jia, and Y. Wan, The Study of the Tribological Properties of TiB<sub>2</sub>/Cr Multilayered Coatings over a Wide Temperature Range, *J. Market. Res.*, 2022, **16**, p 290-301.
23. J.Y. Huang, F. Ding, B.I. Yakobson, P. Lu, L. Qi, and J. Li, In Situ Observation of Graphene Sublimation and Multi-Layer Edge Reconstructions, *Proc. Natl. Acad. Sci.*, 2009, **106**(25), p 10103-10108. <https://doi.org/10.1126/science.1102896>
24. K.S. Novoselov, A.K. Geim, S.V. Morozov, D. Jiang, M.I. Katsnelson, I.V. Grigorieva, S.V. Dubonos, and A.A. Firsov, Two-Dimensional Gas of Massless Dirac Fermions in Graphene, *Nature*, 2005, **438**(7065), p 197-200.
25. C. Gómez-Navarro, M. Burghard, and K. Kern, Elastic Properties of Chemically Derived Single Graphene Sheets, *Nano. Lett.*, 2008, **8**(7), p 2045-2049.
26. I. Taheridoustabad, M. Khosravi, and Y. Yaghoobinezhad, Fabrication of GO/RGO/TiC/TiB<sub>2</sub> Nanocomposite Coating on Ti-6Al-4V Alloy Using Electrical Discharge Coating and Exploring Its Tribological Properties, *Tribol. Int.*, 2021, **156**, p 106860.
27. C. Lee, X. Wei, J.W. Kysar, and J. Hone, Measurement of the Elastic Properties and Intrinsic Strength of Monolayer Graphene, *Science*, 2008, **321**(5887), p 385-388. <https://doi.org/10.1126/science.1157996>
28. J.S. Bunch, S.S. Verbridge, J.S. Alden, A.M. Van Der Zande, J.M. Parpia, H.G. Craighead, and P.L. McEuen, Impermeable Atomic Membranes from Graphene Sheets, *Nano. Lett.*, 2008, **8**(8), p 2458-2462. <https://doi.org/10.1021/nl801457b>
29. F. Yanhan, F. Jianhua, L. Ping, G. Kecheng, S. Shuang, W. Jiang, and J. Zeqi, Preparation and Tribological Behaviors of Plasma Sprayed NiAl-Cu/Graphite Nanosheets Composite Coating, *Tribol. Int.*, 2022, **167**, p 107360.
30. M. Schriver, W. Regan, W.J. Gannett, A.M. Zaniwski, M.F. Crommie, and A. Zettl, Graphene as a Long-Term Metal Oxidation Barrier: Worse Than Nothing, *ACS Nano*, 2013, **7**(7), p 5763-5768. <https://doi.org/10.1021/nn4014356>

31. D. Kang, J.Y. Kwon, H. Cho, J.H. Sim, H.S. Hwang, C.S. Kim, and H.S. Shin, Oxidation Resistance of Iron and Copper Foils Coated with Reduced Graphene Oxide Multilayers, *Acs Nano*, 2012, **6**(9), p 7763-7769. <https://doi.org/10.1021/nn30171316>
32. H. Yamaguchi, J. Granstrom, W. Nie, H. Sojoudi, T. Fujita, D. Voiry, and M. Chhowalla, Reduced Graphene Oxide Thin Films as Ultrabarriers for Organic Electronics, *Adv. Energy Mater.*, 2014, **4**(4), p 1300986. <https://doi.org/10.1002/aenm.201300986>
33. D. Prasai, J.C. Tuberquia, R.R. Harl, G.K. Jennings, B.R. Rogers, and K.I. Bolotin, Graphene: Corrosion-Inhibiting Coating, *ACS Nano*, 2012, **6**(2), p 1102-1108.
34. R.R. Nair, H.A. Wu, P.N. Jayaram, I.V. Grigorieva, and A.K. Geim, Unimpeded Permeation of Water Through Helium-Leak-Tight Graphene-Based Membranes, *Science*, 2012, **335**(6067), p 442-444. <https://doi.org/10.1126/science.1211694>
35. R.K. Joshi, P. Carbone, F.C. Wang, V.G. Kravets, Y. Su, I.V. Grigorieva, and R.R. Nair, Precise and Ultrafast Molecular Sieving Through Graphene Oxide Membranes, *Science*, 2014, **343**(6172), p 752-754. <https://doi.org/10.1126/science.1245711>
36. Y.-P. Hsieh, M. Hofmann, K.-W. Chang, J.G. Jhu, Y.-Y. Li, K.Y. Chen, C.C. Yang, W.-S. Chang, and L.-C. Chen, Complete Corrosion Inhibition through Graphene Defect Passivation, *ACS Nano*, 2014, **8**(1), p 443-448.
37. J.H. Park and J.M. Park, Electrophoretic Deposition of Graphene Oxide on Mild Carbon Steel for Anti-Corrosion Application, *Surf. Coat. Technol.*, 2014, **254**, p 167-174. <https://doi.org/10.1016/j.surfcoat.2014.06.007>
38. A. Raslan, L. Saenz del Burgo, J. Ciriza, and J.L. Pedraz, Graphene Oxide and Reduced Graphene Oxide-Based Scaffolds in Regenerative Medicine, *Int. J. Pharm.*, 2020, **580**, p 119226.
39. P.F. Li, H. Zhou, and X. Cheng, Investigation of a Hydrothermal Reduced Graphene Oxide Nano Coating on Ti Substrate and Its Nano-Tribological Behavior, *Surf. Coat. Technol.*, 2014, **254**, p 298-304. <https://doi.org/10.1016/j.surfcoat.2014.06.038>
40. N. Cao and Y. Zhang, Study of Reduced Graphene Oxide Preparation by Hummers' Method and Related Characterization, *J. Nanomater. Hindawi*, 2015, **2015**, p e168125. <https://doi.org/10.1155/2015/168125>
41. K.H. Lee, B. Lee, S.-J. Hwang, J.-U. Lee, H. Cheong, O.-S. Kwon, K. Shin, and N.H. Hur, Large Scale Production of Highly Conductive Reduced Graphene Oxide Sheets by a Solvent-Free Low Temperature Reduction, *Carbon*, 2014, **69**, p 327-335.
42. A.K. Keshri, R. Patel, and A. Agarwal, Comprehensive Process Maps to Synthesize High Density Plasma Sprayed Aluminum Oxide Composite Coatings with Varying Carbon Nanotube Content, *Surf. Coat. Technol.*, 2010, **205**(3), p 690-702. <https://doi.org/10.1016/j.surfcoat.2010.07.007>
43. A.K. Keshri and A. Agarwal, Wear Behavior of Plasma-Sprayed Carbon Nanotube-Reinforced Aluminum Oxide Coating in Marine and High-Temperature Environments, *J. Therm. Spray Tech.*, 2011, **20**(6), p 1217-1230. <https://doi.org/10.1007/s11666-011-9669-2>
44. V. Bolleddu, V. Racherla, and P.P. Bandyopadhyay, Microstructural Characterization of Plasma Sprayed Conventional and Nanostructured Coatings with Nitrogen as Primary Plasma Gas, *Surf. Coat. Technol.*, 2013, **235**, p 424-432. <https://doi.org/10.1016/j.surfcoat.2013.07.069>
45. J. Shen, Y. Hu, C. Li, C. Qin, and M. Ye, Synthesis of Amphiphilic Graphene Nanoplatelets, *Small*, 2009, **5**(1), p 82-85. <https://doi.org/10.1002/sml.200800988>
46. P.K. Aw, A.L.K. Tan, T.P. Tan, and J. Qiu, Corrosion Resistance of Tungsten Carbide Based Cermet Coatings Deposited by High Velocity Oxy-Fuel Spray Process, *Thin Solid Films*, 2008, **516**(16), p 5710-5715. <https://doi.org/10.1016/j.tsf.2007.07.065>
47. G.M.T. Basha and B. Venkateshwarlu, Influence of Carbon Nanotubes Reinforcement on Characteristics of Thermally Sprayed Ceramic Coatings, *Surf. Rev. Lett.*, 2021, **28**(02), p 2050052. <https://doi.org/10.1142/S0218625X20500523>
48. A.K. Keshri and A. Agarwal, Splat Morphology of Plasma Sprayed Aluminum Oxide Reinforced with Carbon Nanotubes: A Comparison between Experiments and Simulation, *Surf. Coat. Technol.*, 2011, **206**(2), p 338-347. <https://doi.org/10.1016/j.surfcoat.2011.07.025>
49. S.C. Jambagi, A. Agarwal, N. Sarkar, and P.P. Bandyopadhyay, Plasma-Sprayed Titania and Alumina Coatings Obtained from Feedstocks Prepared by Heterocoagulation with 1 Wt.% Carbon Nanotube, *J. Mater. Eng. Perform.*, 2018, **27**(5), p 2364-2372. <https://doi.org/10.1007/s11665-018-3319-5>
50. E.H. Jordan, M. Gell, Y.H. Sohn, D. Goberman, L. Shaw, S. Jiang, M. Wang, T.D. Xiao, Y. Wang, and P. Strutt, Fabrication and Evaluation of Plasma Sprayed Nanostructured Alumina-Titania Coatings with Superior Properties, *Mater. Sci. Eng. A*, 2001, **301**(1), p 80-89. [https://doi.org/10.1016/S0921-5093\(00\)01382-4](https://doi.org/10.1016/S0921-5093(00)01382-4)
51. H. Luo, D. Goberman, L. Shaw, and M. Gell, Indentation Fracture Behavior of Plasma-Sprayed Nanostructured Al<sub>2</sub>O<sub>3</sub>-13wt%TiO<sub>2</sub> Coatings, *Mater. Sci. Eng. A*, 2003, **346**(1), p 237-245. [https://doi.org/10.1016/S0921-5093\(02\)00523-3](https://doi.org/10.1016/S0921-5093(02)00523-3)
52. I. Ahmad, M. Islam, T. Subhani, and Y. Zhu, Characterization of GNP-Containing Al<sub>2</sub>O<sub>3</sub> Nanocomposites Fabricated via High Frequency-Induction Heat Sintering Route, *J. Mater. Eng. Perform.*, 2015, **24**(11), p 4236-4243. <https://doi.org/10.1007/s11665-015-1738-0>
53. S.T. Aruna, N. Balaji, J. Shedthi, and V.K.W. Grips, Effect of Critical Plasma Spray Parameters on the Microstructure, Microhardness and Wear and Corrosion Resistance of Plasma Sprayed Alumina Coatings, *Surf. Coat. Technol.*, 2012, **208**, p 92-100. <https://doi.org/10.1016/j.surfcoat.2012.08.016>
54. X. Lin, Y. Zeng, X. Zhou, and C. Ding, Microstructure of Alumina-3wt.% Titania Coatings by Plasma Spraying with Nanostructured Powders, *Mater. Sci. Eng. A*, 2003, **357**(1), p 228-234. [https://doi.org/10.1016/S0921-5093\(03\)00164-3](https://doi.org/10.1016/S0921-5093(03)00164-3)
55. B. Normand, V. Fervel, C. Coddet, and V. Nikitine, Corrigendum to "Tribological properties of plasma sprayed alumina-titania coatings: role and control of the microstructure": [Surf. Coat. Technol. 123, 278-287], *Surf. Coat. Technol.*, 2000, **2**(127), p 284. [https://doi.org/10.1016/S0257-8972\(00\)00702-7](https://doi.org/10.1016/S0257-8972(00)00702-7)
56. B. Mukherjee, O.A. Rahman, M. Sribalaji, S.R. Bakshi, and A.K. Keshri, Synergistic Effect of Carbon Nanotube as Sintering Aid and Toughening Agent in Spark Plasma Sintered Molybdenum Disilicide-Hafnium Carbide Composite, *Mater. Sci. Eng. A*, 2016, **678**, p 299-307. <https://doi.org/10.1016/j.msea.2016.10.009>
57. A. Nieto, D. Lahiri, and A. Agarwal, Synthesis and Properties of Bulk Graphene Nanoplatelets Consolidated by Spark Plasma Sintering, *Carbon*, 2012, **50**(11), p 4068-4077. <https://doi.org/10.1016/j.carbon.2012.04.054>
58. B. Mukherjee, O.A. Rahman, A. Islam, M. Sribalaji, and A.K. Keshri, Plasma Sprayed Carbon Nanotube and Graphene Nanoplatelets Reinforced Alumina Hybrid Composite Coating with Outstanding Toughness, *J. Alloys Compd.*, 2017, **727**, p 658-670. <https://doi.org/10.1016/j.jallcom.2017.08.160>
59. S. Singh, K.K. Pandey, O.A. Rahman, S. Haldar, D. Lahiri, and A.K. Keshri, Investigation of Crystallinity, Mechanical Properties, Fracture Toughness and Cell Proliferation in Plasma Sprayed Graphene Nano Platelets Reinforced Hydroxyapatite Coating, *Mater. Res. Express*, 2020, **7**(1), p 015415. <https://doi.org/10.1088/2053-1591/ab6c23>
60. J.E. Terpero, S. Namin, D. Lahiri, K. Balani, N. Tsoukias, and A. Agarwal, Effect of Carbon Nanotube and Aluminum Oxide Addition on Plasma-Sprayed Hydroxyapatite Coating's Mechanical Properties and Biocompatibility, *Mater. Sci. Eng. C*,

- 2009, **29**(7), p 2195-2202. <https://doi.org/10.1016/j.msec.2009.05.001>
61. M. Kašparová, F. Zahálka, and Š. Houdková, Evaluation of the Bond Strength of the Thermally Sprayed Coatings, MeTal, 2010, 18.-20.5.2010, Roznov pod Radhostem, Czech Republic, EU
62. M.P. Schmitt, A.K. Rai, R. Bhattacharya, D. Zhu, and D.E. Wolfe, Multilayer Thermal Barrier Coating (TBC) Architectures Utilizing Rare Earth Doped YSZ and Rare Earth Pyrochlores, *Surf. Coat. Technol.*, 2014, **251**, p 56-63. <https://doi.org/10.1016/j.surfcoat.2014.03.049>
63. J. Stokes and L. Looney, Residual Stress in HVOF Thermally Sprayed Thick Deposits, *Surf. Coat. Technol.*, 2004, **177-178**, p 18-23. <https://doi.org/10.1016/j.surfcoat.2003.06.003>

**Publisher's Note** Springer Nature remains neutral with regard to jurisdictional claims in published maps and institutional affiliations.

Springer Nature or its licensor (e.g. a society or other partner) holds exclusive rights to this article under a publishing agreement with the author(s) or other rightsholder(s); author self-archiving of the accepted manuscript version of this article is solely governed by the terms of such publishing agreement and applicable law.